

See discussions, stats, and author profiles for this publication at: <https://www.researchgate.net/publication/365086717>

Visualization of Sub-Nanometer Scale Multi-Orientational Ordering in Thin Films of Polymer/Non-Fullerene Acceptor Blends

Article in *Journal of Materials Chemistry A* · January 2022

DOI: 10.1039/D2TA05083H

CITATIONS

0

READS

34

9 authors, including:



Urvashi Bothra

IITB-Monash Research Academy

9 PUBLICATIONS 35 CITATIONS

[SEE PROFILE](#)



Wen Liang Tan

Monash University (Australia)

47 PUBLICATIONS 837 CITATIONS

[SEE PROFILE](#)



Hariprasad Venugopal

Monash University (Australia)

60 PUBLICATIONS 1,204 CITATIONS

[SEE PROFILE](#)



Chandramouli Subramaniam

Indian Institute of Technology Bombay

79 PUBLICATIONS 1,681 CITATIONS

[SEE PROFILE](#)

Some of the authors of this publication are also working on these related projects:



Transistors and flexible electronics applied nanotechnology [View project](#)



Organic thin film transistors [View project](#)



Cite this: DOI: 10.1039/d2ta05083h

Visualization of sub-nanometer scale multi-orientational ordering in thin films of polymer/non-fullerene acceptor blends†

Urvashi Bothra,^{a,b,c} Pramiti Hui,^d Wen Liang Tan,^c Eliot Gann,^e
Hariprasad Venugopal,^f Chandramouli Subramaniam,^g Amelia C. Y. Liu,^{h,*g}
Christopher R. McNeill^{i,*c} and Dinesh Kabra^{i,*b}

Improvement in the efficiency of organic photovoltaics (OPVs) is mainly attributed to non-fullerene acceptors (NFAs). However, NFAs exhibit an anisotropic chemical structure, resulting in over-sized aggregation, which can affect the exciton dissociation and charge transport. While the effect of different morphologies on the device performance has been observed in several studies, little is known about the composition and local molecular ordering in bulk heterojunction (BHJ) blend films of the polymer donor and NFAs. Here, we manipulate the morphology of blend films from large micron-sized phase-separated domains to fine-scale nano-domains via varying the drying kinetics of the film formation. We investigate the composition by micro-Raman spectroscopic studies of these blend films and visualize the molecular ordering at the sub-nanometer scale using a combination of cryo-electron microscopy and X-ray studies. Interestingly, we find that the molecules are oriented differently at the edge and at the center of these domains, a feature that has not been observed previously in spin-coated films containing NFAs. Moreover, we have extended our study to other donor-NFA systems and have observed a similar effect of drying kinetics on the microstructural and optical properties. Furthermore, our study shows that the change in the performance of the PTB7-Th:IEICO-4F device due to micron- and nano-sized morphology is relatively less, which is in contrast to a general notion of OPV systems.

Received 26th June 2022
Accepted 1st November 2022

DOI: 10.1039/d2ta05083h

rsc.li/materials-a

Introduction

The development of NFAs along with new polymeric donors has resulted in a drastic increase in the efficiency of binary and ternary organic solar cells (OSCs),^{1–3} with a current reported record power conversion efficiency of 19%.⁵⁶ The major advantages of NFAs include improved absorption in the near-infrared region due to a tunable bandgap, efficient exciton dissociation with low energy offsets, and improved stability.^{4–8} The advent of

NFAs has also resulted in unexpected observations such as intra-moiety excimer states that can exist in a single-component and barrierless free-charge generation in BHJ solar cells, which are still not completely understood.^{9–11} NFAs also exhibit strong self-assembly and molecular stacking, which can result in over-sized phase separation and tends to negatively affect photoinduced charge generation and interpenetrating transport pathways in the devices.^{12,13} Therefore, to understand the device physics of NFAs and to improve the device efficiency further, it is critical to examine the BHJ morphology of NFAs in detail.

Due to their core unit, side chains, and terminating units, NFAs exhibit various molecular packing configurations that range from highly structured lamellar crystals to π - π stacking.^{12,14,15} The various molecular packing configurations of NFAs include H aggregation, J aggregation, and cluster formation, which modifies the domain size and domain purity, hence influencing charge dissociation and transport in devices.^{16,17} The critical parameters by which morphology can be tuned are chemical structures and processing conditions. For instance, the molecular packing of the acceptor IDTT-CX-TIC changed from π - π stacking to non-stacking mode when the side chain is varied from C6 to C10, which led to an increase of 3% in efficiency.¹⁸ Recent studies on NFAs have also shown that processing conditions have a strong influence on morphology.^{4,19–21}

^aIITB-Monash Research Academy, IIT Bombay, Mumbai, 400076, India

^bDepartment of Physics, Indian Institute of Technology Bombay, Powai, Mumbai, 400076, India. E-mail: dkabra@iitb.ac.in

^cDepartment of Materials Science and Engineering, Monash University, Wellington Road, Clayton, Victoria, 3800, Australia. E-mail: christopher.mcneill@monash.edu

^dDepartment of Chemistry, Indian Institute of Technology Bombay, Powai, Mumbai, 400076, India. E-mail: csbbu@chem.iitb.ac.in

^eMaterials Measurement Science Division, National Institute of Standards and Technology, Gaithersburg, MD 20899, USA

^fRamaciotti Centre for Cryo-Electron Microscopy, Monash University, Clayton, Victoria 3800, Australia

^gSchool of Physics and Astronomy, Monash University, Clayton, Victoria, 3800, Australia. E-mail: amelia.liu@monash.edu

† Electronic supplementary information (ESI) available. See DOI: <https://doi.org/10.1039/d2ta05083h>

Xu *et al.* showed the effect of time-dependent molecular aggregation of PM6:BTP-BO-4Cl on solar cell performance due to delayed processing conditions.²² In another interesting study, Xian *et al.* performed time-dependent microstructural studies to understand the effect of thermal annealing duration on the P3HT:ZY-4Cl blend morphology.²³ Therefore, since NFAs can exhibit a range of different molecular packing configurations, it is critical to find a suitable donor material and tune the processing conditions to improve the performance of the device further.

The thermodynamic conditions and kinetics of solvent evaporation during processing affect the morphology of BHJ blends at multiple length scales.^{20,24–32} Large-scale phase-separated morphologies have been observed for many polymer/polymer and polymer/fullerene systems.^{33–36} Due to the crystallisation of both donor polymer and NFA, phase separations into amorphous polymer/crystalline NFA and semi-crystalline polymer/crystalline NFA can take place. A correlated orientation of donor and acceptor molecules at the BHJ can improve the free charge carrier separation.³⁷ Furthermore, the molecular orientation of the donor and the NFA with respect to the electrode is one of the most important factors determining charge transport. However, the visualization of molecular orientations of the donor and the NFA is difficult due to the similarities in their chemical and electronic structures. Köntges *et al.*, for example, visualized the molecular arrangement in PBDB-T:ITIC blends by using electron energy loss spectroscopy in conjunction with transmission electron microscopy, showing the presence of adjacent donor and acceptor crystals in the blend, which can be identified as a key factor for efficient exciton dissociation in D–A systems with small energy offset.³⁸ Therefore, a detailed understanding of the complex morphology of the NFAs and their blends is required to answer various questions in the domain of OSCs.

In this work, we present a detailed study of the visualization of the micro- and nanoscale morphologies of the low bandgap NFA **IEICO-4F** and donor polymer **PTB7-Th**. The morphology of the **PTB7-Th:IEICO-4F** blend is tuned from a large-scale phase-separated morphology with features on the micron scale to a fine morphology with nanoscale phase separation by varying either the spin-coating speed or spin-coating duration. From micro-Raman spectroscopy, we find that in films with a coarse morphology, the domains are highly ordered and rich in **IEICO-4F**, whereas the surrounding matrix is rich in **PTB7-Th**. Furthermore, the aggregation of **IEICO-4F** molecules in the coarser morphology leads to a red-shift in the absorption edge and decrease in oscillator strength. Data from grazing incidence wide-angle X-ray scattering (GIWAXS) show that the film with a fine morphology possesses a preferential crystallite orientation, whereas films with a coarse morphology are less textured. Interestingly, from cryo-electron microscopy (cryo-EM) analysis, we find that **IEICO-4F** crystallites align with different orientations at the edge and the center of the micron-scale domains, a feature which has not been observed thus far. These observations could provide a new possible mechanism for efficient charge separation in single-component NFAs due to the

possibility of different electrostatics (different HOMO and LUMO levels) that is induced by different molecular orientations.^{10,11,39}

Results and discussion

Optical properties

The chemical structures of **IEICO-4F** and **PTB7-Th** are shown in Fig. 1(a). **PTB7-Th:IEICO-4F** blend solutions were prepared using chlorobenzene (CB) as the major solvent with 3 vol% 1-chloronaphthalene (1-CN) as the solvent additive. Fig. 1(b) shows the absorption spectra of blend films with a weight ratio of 1:2 donor–acceptor (D–A), which were spin-coated at 1500 rpm for different spin-coating durations. The films that were spin-coated for longer durations show increased absorption, especially 800 nm onwards associated with **IEICO-4F**. However, there is no change in absorption spectra on varying spin duration when the blend ratio is changed to 4:1, as shown in Fig. 1(c). Similarly, Fig. S1(a)–(c)† shows the absorption spectra of films for other D–A ratios (1:1.5, 1:1, and 2:1), which were spin-coated at 1500 rpm for 30 seconds and 120 seconds. This spin-coating-induced change in the absorption spectra is observed only when the acceptor amount is equal to or higher than the donor amount. To obtain a film thickness of ≈ 90 nm in all the films, the solution concentration for blends with weight ratios of 1:2, 1:1.5, and 1:1 was set at 20 mg ml^{-1} , while for blends with weight ratios of 2:1 and 4:1, it was set at 15 mg ml^{-1} . Due to the complimentary absorption spectra of the pristine materials, the dominant absorption peak of the blend changes from **IEICO-4F** to **PTB7-Th** on varying the blend ratio from 1:2 to 4:1. Fig. 1(d) shows the normalized absorption spectra of pristine **PTB7-Th** and pristine **IEICO-4F** films along with that of blend films that were spin-coated for 30 seconds and 120 seconds. Blend films spin-coated for 30 seconds show a red-shifted absorption edge for **IEICO-4F**. The slow drying associated with spin-coating for a shorter duration promotes increased molecular aggregation in the film. Since 1-CN is a high-boiling-point solvent (B.P. of 1-CN 263°C , B.P. of CB 132°C), and likely to remain longer in the film and promote aggregation, films were prepared by spin-coating neat **IEICO-4F** from either CB or CB with 3 vol% 1-CN. The addition of 1-CN is seen to change the absorption spectra of neat **IEICO-4F** by broadening the spectra in both lower and higher wavelength regions as shown in the inset of Fig. 1(d).

The absorption spectra of **PTB7-Th:IEICO-4F** shown in Fig. 1 do not converge to zero because of the prominent total reflection (reflection and scattering) by the blend system. The total reflection of **PTB7-Th:IEICO-4F** blend (1:2) films spin-coated at 1500 rpm for 30 seconds and 120 seconds is shown in Fig. S2(a)† where a peak reflection is observed after 900 nm for both the films. Fig. S2(c)† shows the absorbance for both the films, which is a fraction of total light absorbed by the sample. Therefore, the absorption spectra shown in Fig. 1 and S1† have contribution from reflectance and scattering also. The absorption cross-section (σ) of pristine **IEICO-4F** with and without CN in CB and for the blends processed at different durations is shown in Fig. S3.† The absorption cross-section, σ , of **IEICO-4F**

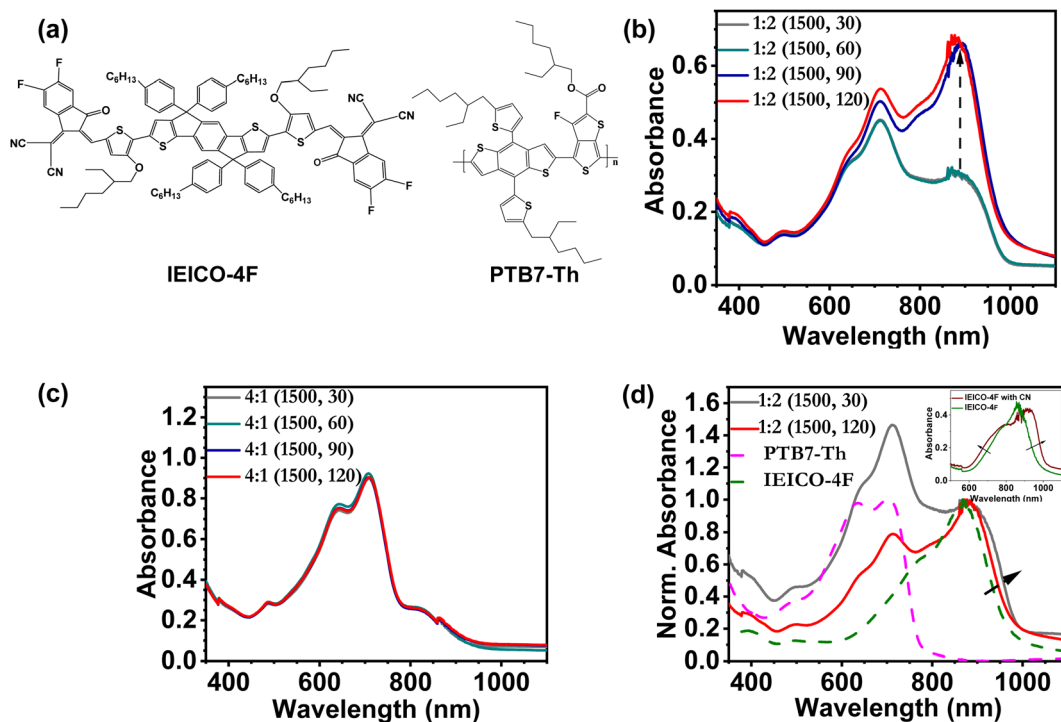


Fig. 1 Chemical structure and absorption spectra of pristine and blend films. (a) The chemical structure of IEICO-4F and PTB7-Th. Absorption spectra of PTB7-Th:IEICO-4F film for blend ratios of (b) 1 : 2 and (c) 4 : 1, spin-coated at 1500 rpm for 30 seconds to 120 seconds. (d) Normalized absorption spectra of pristine PTB7-Th (magenta dash line), IEICO-4F (olive dash line), and PTB7-Th:IEICO-4F blend film at a 1 : 2 ratio spin-coated at 1500 rpm for 30 and 120 seconds. Inset shows absorption spectra of pristine IEICO-4F in CB (olive solid line) and IEICO-4F in CB with 3 vol% 1-CN (wine solid line).

spin-coated with CN film is lower compared to that of IEICO-4F spin-coated without the solvent additive. Similarly, the absorption cross-section characteristics are found to be lower for the coarse blend film than the fine blend film. ESI Note 1† provides further details on the calculation of the absorption cross-section. Thus, the different solvent-drying conditions may alter the molecular packing of IEICO-4F resulting in pronounced changes in optoelectronic properties.

Photoluminescence (PL) spectra of pristine and blend films were recorded with excitation provided by a 638 nm laser. Fig. S4(a) and (b)† shows that films of pristine PTB7-Th in CB and pristine IEICO-4F in CB have a PL peak at 760 nm and 920 nm, respectively. The PL spectrum of blend films shows that the PL from PTB7-Th is mostly quenched and the majority of PL counts are from IEICO-4F (Fig. S4(c)† inset). Comparing the PL of blend films spin-coated at 30 seconds and 120 seconds, the films spin-coated at 120 seconds show a peak at 910 nm whereas films spin-coated for 30 seconds show increased PL counts along with a red-shift in the PL spectra (Fig. S4(c)†). The increased PL-quenching in blend films spin-coated for 120 seconds indicates reduced geminate recombination due to the presence of increased interfacial area between donor and acceptor materials.

Phase separated morphology

To investigate the mechanism behind the change in absorption due to different processing conditions, the morphology of the

blend films has been studied. Fig. S5† shows digital images of blend films that were spin-coated with different donor-acceptor ratios and processed at varied spin speeds and spin durations. Films with 1 : 2 and 1 : 1.5 blend ratios that were spin-coated at a lower speed or shorter spin duration show a matte finish, which changes to a shiny finish at a higher speed or longer spin duration. However, no change in the appearance of the film spin-coated with different spin speeds or durations is visible with blend ratios of 2 : 1 and 4 : 1. Therefore, to study the morphology of these films in detail, atomic force microscopy (AFM) was performed.

Fig. 2 shows the tapping-mode AFM images of ≈ 90 nm-thick PTB7-Th:IEICO-4F (1 : 1.5) blend films that were spin-coated at different spin speeds and for different spin durations. The first column on the left, in Fig. 2(a)–(d) shows films spin-coated at 1000 rpm with spin duration varying from 30 seconds (top) to 120 seconds (bottom). The middle column similarly shows films spin-coated at 1500 rpm for different durations (30 seconds top to 120 seconds bottom) and the column on the right shows films spin-coated at 2000 rpm. The AFM images show a coarse lateral phase-separated morphology with a root mean square (RMS) roughness of 29–40 nm for films that were spin-coated for a short duration or low speed. The films that exhibit this coarse morphology also exhibited a matte finish optically. Films that showed a shiny finish visually are found to exhibit a fine-scale morphology from AFM, with a RMS roughness of 3–4 nm. Fig. S6† displays AFM height images of blend films with

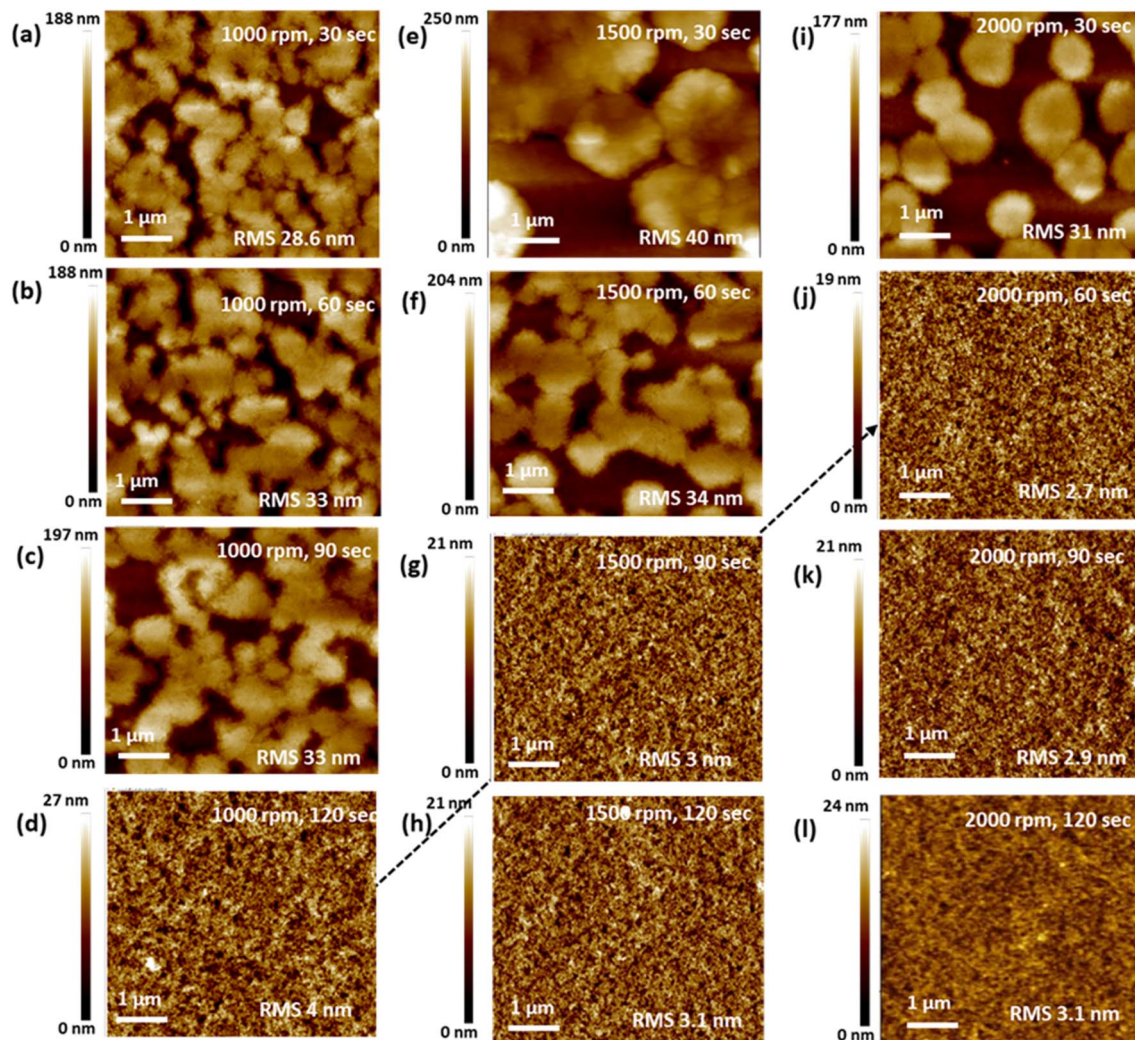


Fig. 2 Morphological image of PTB7-Th:IEICO-4F blend films. The atomic force microscopy (AFM) image of 1 : 1.5 PTB7-Th:IEICO-4F films spin-coated at (a)–(d) 1000 rpm, (e)–(h) 1500 rpm, and (i)–(l) 2000 rpm for different durations of spin-coating (30 s, 60 s, 90 s, and 120 s) (5 μm \times 5 μm).

different D–A ratios, which were spin-coated for either 30 or 120 seconds. These AFM images demonstrate the growth of large domains when the donor concentration is lower than the acceptor concentration in the blend. It is also observed that the phase-separated domain size is gradually decreased as the donor fraction in the blend is increased.

Films that were spin-coated at either a slow speed or for a shorter duration do not dry immediately, which promotes molecular aggregation and the formation of a micron-sized phase-separated morphology. The degree of phase separation observed and its dramatic transition could be due to the hypo-miscibility of IEICO-4F in PTB7-Th, which can result in over-purification of the domains.⁴⁰ The observed aggregation in the blend films reduces interfacial area between donor and acceptor materials, which accounts for the observed increase in PL counts in phase-separated films (Fig. S4c†). Henceforth, the blend films that are spin-coated for a short duration will be referred to as “coarse” and those that are spin-coated for longer duration as “fine.”

Fig. S7† shows the AFM height and phase images of pristine IEICO-4F films that were spin-coated either from neat CB or from CB with 3 vol% 1-CN. The IEICO-4F film processed with 1-CN shows large domains of a size $\approx 10 \mu\text{m}$ and RMS roughness of 135 nm, whereas the films without 1-CN show a roughness of 11 nm. Fig. S8† compares the 2D and 3D height images of a coarse blend film with a pristine film of IEICO-4F processed with 1-CN. Both films show a similar phase-separated morphology with large aggregated features due to protracted drying of the film in a high-boiling-point solvent additive, but with a reduced domain size for the blend film. It should also be noted that the AFM images of the coarse blend film and pristine IEICO-4F film processed from 1-CN show a radial contrast within the circular domains. From the AFM height image and observations of the *in situ* drying of the blend film (Video S1 and S2†), we hypothesize that the coarse phase separation during drying takes place through a nucleation and growth process, resulting in micron-sized circular domains. The decrease in the

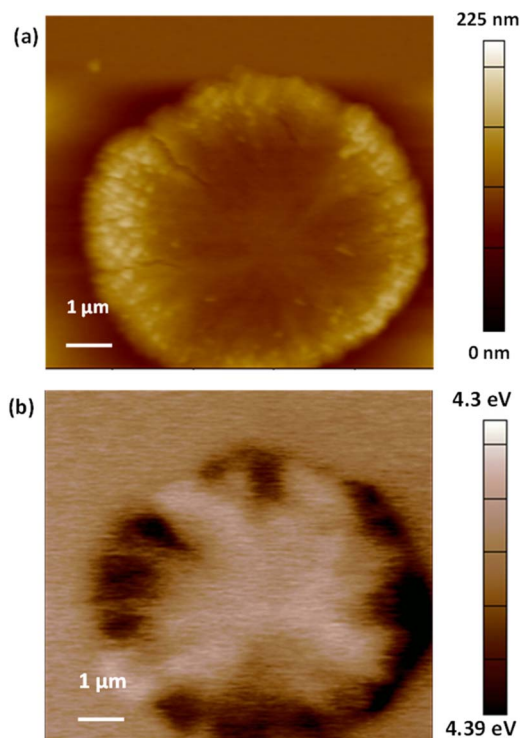


Fig. 3 Morphology and potential image of the PTB7-Th:IEICO-4F blend film. (a) The height image (AFM) and (b) KPFM potential image of the 1:1.5 PTB7-Th:IEICO-4F film spin-coated at 1500 rpm, 30 seconds on precleaned ITO-coated glass substrates. The calculated work function of Ti/Ir tip is 4.46 eV.

domain size for the blend films compared to the pristine films could be due to restricted nucleation of pristine IEICO-4F by the addition of PTB7-Th, which results in different morphologies due to different drying kinetics of the film.

Kelvin probe force microscopy (KPFM) was performed to study the composition within the phase-separated domains of the BHJ morphology.^{41–44} Fig. 3 shows AFM and the KPFM images of the coarse blend film. The detailed information and formulae used to determine the work function of the components are provided in ESI Note 2 and Fig. S9.† Fig. 3(b) shows that the edges of the circular domains exhibit a higher work function (W.F.) with the center of the domain exhibiting a lower W.F. The surrounding matrix region shows a W.F. intermediate to the center and edges of the circular domain. From these observations along with the W.F. of pristine materials, we infer the presence of a capping layer of PTB7-Th covering the center of the circular domains but with areas at the edge, where crystallites of IEICO-4F penetrate through. This assignment is consistent with the morphology seen with AFM, with a smoother surface texture seen in the center of the domain and a coarser, nodular texture seen at the edges of the domain.

Micro-spectroscopic studies

To provide an unambiguous assignment of the relative composition of the observed domains in coarse PTB7-Th:IEICO-4F blend films, μ -Raman spectroscopy was performed³⁴ with an

excitation wavelength of 632.8 nm laser (He-Ne laser). Fig. 4(a) shows the optical image of the PTB7-Th:IEICO-4F blend with a 1:1.5 weight ratio spin-coated for 30 seconds. μ -Raman spectroscopy was performed for pristine PTB7-Th and pristine IEICO-4F to provide the reference spectra of neat materials and performed on “matrix” and “domain” regions of the coarse blend film as identified in Fig. 4(a). The schematic of the μ -Raman setup is shown in Fig. 4(b). Fig. 4(c) shows normalized μ -Raman spectra of pristine and blend films. The Raman spectrum of pristine PTB7-Th resembles the spectrum reported by Kim *et al.* with peak positions at 1467 cm^{-1} , 1494 cm^{-1} , and 1521 cm^{-1} , which corresponds to CC stretching modes in the BDT backbone and side chain unit.⁴⁵ Furthermore, the prominent peaks of IEICO-4F pristine film are at 1368 cm^{-1} , 1400 cm^{-1} , and 1602 cm^{-1} . The vibrational signatures of PTB7-Th are observed in both the domain and matrix regions of the blend film at 1467 cm^{-1} , 1494 cm^{-1} , and 1521 cm^{-1} . However, the characteristic peaks of IEICO-4F (1310 cm^{-1} , 1368 cm^{-1} , and 1400 cm^{-1}) are strongly manifested in the domain region when compared to the matrix region. Therefore, we understand that (i) the domains are rich in IEICO-4F and the matrix region is rich in PTB7-Th. (ii) PTB7-Th and IEICO-4F both are present in the domain and matrix regions, which is observed from Fig. S10.† Fig. S10† shows the signature of a few IEICO-4F peaks (1310 cm^{-1} and 1400 cm^{-1}) in the matrix region of the blend film. We note that not all the characteristic peaks of IEICO-4F are present in the matrix region, which could be due to (i) relatively low amount of IEICO-4F in the matrix region and (ii) absence of a few vibrational modes of IEICO-4F in the matrix region due to possibly different molecular packing of isolated IEICO-4F molecules in the PTB7-Th-rich matrix. Hence, additional evidence to confirm the presence of IEICO-4F in matrix region is established in cryo-EM studies (Fig. S16†). Thus, the μ -Raman results identify the relative composition of the donor/acceptor molecules in both the domain and matrix regions.

In order to further understand the molecular ordering of these molecules within the domain and matrix phases, we performed polarization-dependent μ -Raman spectroscopy. Fig. S11† shows polarization-angle-dependent μ -Raman spectra of the domain and matrix regions of the film. A significant angle-dependent intensity profile is observed for various Raman peaks (1310 cm^{-1} , 1368 cm^{-1} , and 1400 cm^{-1}) in the domain region, which intrinsically originates from the molecular ordering leading to orientation of IEICO-4F in this region. Fig. 4(d) presents the normalized Raman intensity for domain and matrix regions at different polarization angles, estimated for one of these Raman intensity shifts. The variation in Raman intensity with polarization angle is much stronger inside the domains than outside, indicating that the IEICO-4F molecules show more pronounced molecular orientational ordering in the enclosed IEICO-4F-rich domains. It is important to note that we cannot comment on the intermixing of PTB7-Th with IEICO-4F for these films from μ -Raman spectroscopy due to the diffraction limit of such measurements; therefore, resonant soft X-ray scattering (R-SoXS) experiment was conducted to obtain nano-scale information.

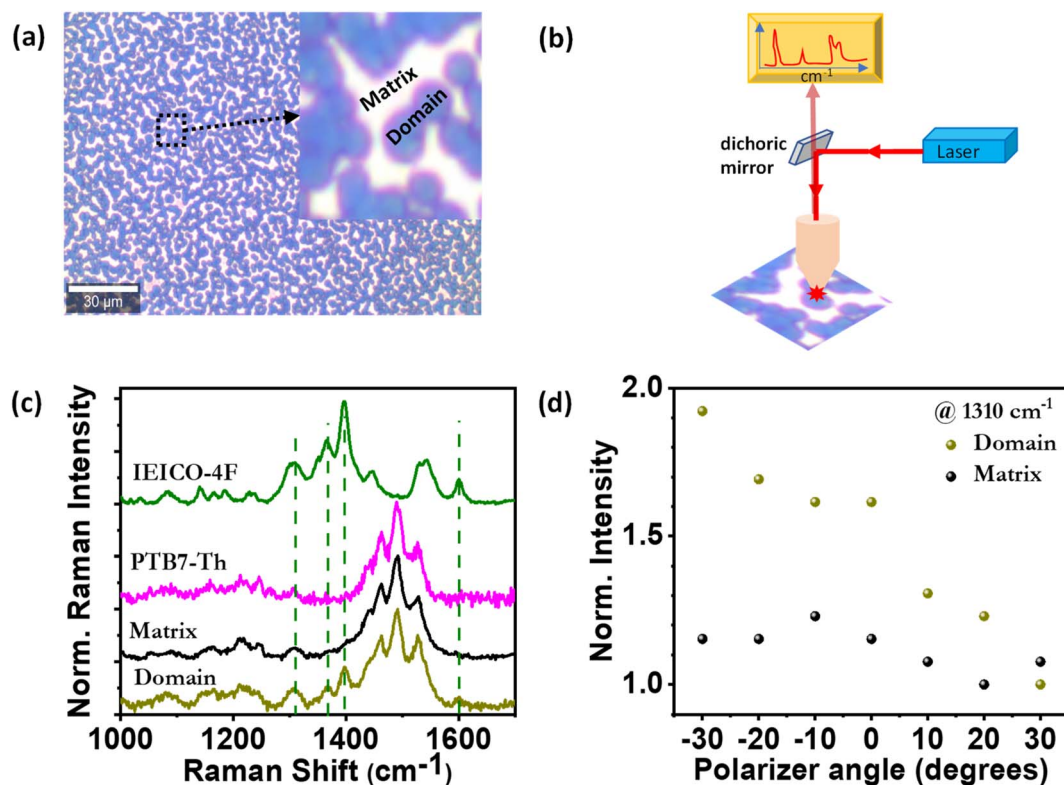


Fig. 4 Micro-Raman spectra of pristine and blend films in domain and matrix regions. (a) The optical image of the 1 : 1.5 PTB7-Th:IEICO-4F film spin-coated at 1500 rpm, 30 seconds. Inset shows the zoomed image representing the inside and outside regions of the film. (b) Schematic of the μ -Raman setup. (c) Normalized Raman intensity for pristine PTB7-Th, pristine IEICO-4F, inside and outside regions of the blend film. (d) Normalized Raman intensity in the inside and outside regions for different polarization angles at 1310 cm^{-1} .

Fig. S12† shows the Lorentz-corrected R-SoXS profiles that were acquired for **PTB7-Th:IEICO-4F** films with different blend ratios spin-coated either at 30 seconds or 120 seconds. From the R-SoXS results, strong scattering is seen at low q for films with the blend ratios of 1 : 1, 1 : 1.5, and 1 : 2 spin-coated at 30 seconds. This strong scattering at low q for these samples is consistent with scattering from large, micron-scale features as seen with AFM. These films with coarse morphology also exhibit scattering at higher q , indicating a hierarchical morphology with spatial fluctuations in composition on sub-micron length scales as well. For the films with blend ratios of 1 : 2, 1 : 1.5, and 1 : 1, when spin-coated at 120 seconds, a strong suppression of scattering at low q is seen, consistent with the transition from a coarse to fine morphology. There are still scattering features seen at intermediate q ($0.001\text{ Å}^{-1} < q < 0.01\text{ Å}^{-1}$) associated with spatial fluctuations in composition on length scales of hundreds of nanometers. While there is certainly a distribution of domain sizes in these samples, there are peaks discernible at $q \approx 0.002\text{ Å}^{-1}$ and $q \approx 0.02\text{ Å}^{-1}$ characteristic of spatial fluctuations on length scales of $\approx 300\text{ nm}$ and $\approx 30\text{ nm}$, respectively. Scattering at $q \approx 0.002\text{ Å}^{-1}$ is most pronounced for the 1 : 1 blend, with similar scattering intensity at $q \approx 0.02\text{ Å}^{-1}$ for the 1 : 2, 1 : 1.5, and 1 : 1 samples. For the 2 : 1 and 4 : 1 blends, there is no change in the R-SoXS scattering profiles with change in spin-speed. Scattering for these two blends is characterized by features above $q \approx 0.01\text{ Å}^{-1}$ consistent with a fine, nanoscale

morphology. The fact that changing the spin-coating speed does not affect the morphology for the 2 : 1 and 4 : 1 blends suggests that at these weight ratios, the concentration of **IEICO-4F** is within the miscibility limit for **IEICO-4F** in **PTB7-Th**. Therefore, the R-SoXS studies corroborate the results that were observed from AFM and absorption spectroscopy; they also provide additional information about the presence of finer domains within the phase-separated region.

Microstructural studies

To elucidate the crystalline nature of the **PTB7-Th:IEICO-4F** blend films, GIWAXS studies were performed. Fig. S13† shows 2D GIWAXS images of pristine films (a)–(c) and blend films (d) and (e). The in-plane (IP) and out-of-plane (OOP) 1-D line profiles for pristine **PTB7-Th**, pristine **IEICO-4F**, pristine **IEICO-4F** processed with 1-CN, and **PTB7-Th:IEICO-4F** blend films with a coarse and fine morphology are shown in Fig. 5(a) and (b). Pristine **PTB7-Th** adopts a face-on orientation with a lamellar stacking (100) peak at 0.265 Å^{-1} and a π - π stacking peak (010) at 1.58 Å^{-1} , which correspond to stacking repeat distances of 23.7 Å and 4.0 Å , respectively.^{46,47} Neat **IEICO-4F** films exhibit a more crystalline nature with many diffraction peaks characteristic of well-defined three-dimensional crystalline order. For the pristine **IEICO-4F** film processed without 1-CN, a random orientation of crystallites is displayed, whereas a more textured orientation is observed for **IEICO-4F** processed

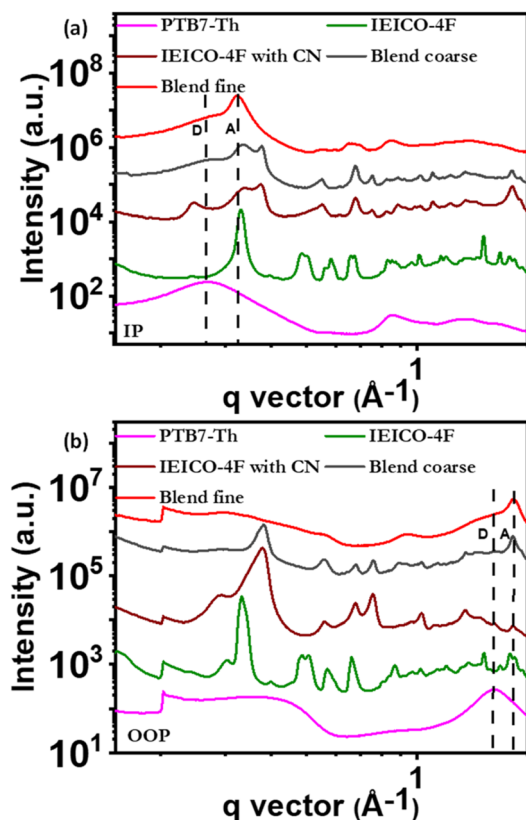


Fig. 5 Structural studies of pristine and blend films. (a) In-plane and (b) out-of-plane GIWAXS line profiles of pristine PTB7-Th, IEICO-4F in CB, IEICO-4F in CB and CN, and coarse blend and fine blend films. The lines are drawn to compare the peaks of blend with the pristine materials. D corresponds to PTB7-Th and A corresponds to IEICO-4F.

with 1-CN. Processing with 1-CN also leads to a different crystalline packing (polymorph) evidenced by the emergence and shifting of diffraction peaks. It is difficult to index the peaks because the crystal structure of IEICO-4F is unknown.

For the blend film with fine morphology, the scattering pattern mostly resembles pristine PTB7-Th with a few additional broad peaks characteristic of IEICO-4F. These IEICO-4F peaks in the fine blend are broader than those seen in neat films and better match the neat film processed without CN. For the coarse blend film, the scattering pattern is dominated by features from crystalline IEICO-4F which match with the peaks of pristine IEICO-4F processed with CN. IEICO-4F crystallites in the coarse blend also show a similar molecular orientation to those in neat films processed with CN. Table S1† shows prominent GIWAXS peaks that correspond to coarse and fine blend morphologies, which are compared with the peaks of pristine films. In general, the GIWAXS results confirm a large difference in the crystalline packing of coarse and blend films, with IEICO-4F being only weakly ordered in films with a fine morphology, and showing a high degree of crystallinity in films with a coarse morphology.

From GIWAXS, information regarding film crystallinity is obtained for the entire blend film. Cryo-EM was also performed, which provides local information about crystallinity and

molecular orientation. Soft materials can be easily damaged by an electron beam; characterization in real space is, therefore, difficult. Cryo-EM provides an excellent characterization technique to study the structural order in soft materials by reducing beam damage on the material.⁴⁸ Fig. S14(a)–(f)† shows the acquired high-magnification cryo-EM image and the corresponding fast Fourier transform (FFT) that were collected for different electron doses. Fig. S14(g)† shows the radial profile of the image FFT collected at different electron doses. Fig. S14(h)† shows the integrated intensity for different spatial frequencies as a function of the electron dose. It can be seen that the peaks in the FFT corresponding to crystalline order do not diminish up to doses of $50 \text{ e}^- \text{ Å}^{-2}$. Therefore, cryo-EM images can be analyzed to understand the local packing of the materials.

Fig. 6(a)–(c) and (d) show high-magnification cryo-EM images of the coarse and fine blends, respectively, acquired at the cross-hair of the low-magnification image present in the inset. Fig. 6(e)–(h) show the high-magnification cryo-EM image from the selected region of Fig. 6(a)–(d), with a scale of 20 nm, along with their FFTs present in the inset. Fig. 6(e)–(h) show the presence of crystalline fringes, which are also represented by the diffraction spot present in the FFT of the image. To visualize the fringes corresponding to the d -spacing of the π - π stacking distance, Fig. 6(e) and (g) are further zoomed to obtain Fig. 6(i) and (j) with a scale of 2 nm. Fig. 6(i) shows crystalline fringes with a spacing of $\sim 0.35 \text{ nm}$ ($\sim q = 1.8 \text{ Å}^{-1}$), which corresponds to the peak of IEICO-4F. Similarly, Fig. 6(j) taken from the outside region of the domain shows crystalline fringes with a d -spacing of $\sim 0.4 \text{ nm}$, which corresponds to the π - π stacking distance of PTB7-Th.

Since both GIWAXS and cryo-EM data of the film provide information regarding interplanar spacing, the q spacings that are obtained from both the techniques should be the same, although there will be some variations in intensity due to the difference between electron and X-ray atomic scattering factors and the contrast transfer function of the TEM.⁴⁹ Fig. 7 shows the comparison of the q values obtained from cryo-EM and GIWAXS for the coarse blend film. The q value that is obtained from the IP GIWAXS line profile coincides with the q value obtained from the radial profile of the FFTs from the different regions of the cryo-EM film, demonstrating good correspondence between the results of GIWAXS and cryo-EM.

Fig. 6(e) and (f) present high-magnification images and their FFT at the edge and the center of the domain, respectively. It is interesting to note that the molecular packing of materials, which is observed at the edge and the center, is mostly complimentary to each other; this is observed in Fig. 7 and Table S2.† For example, the q value of GIWAXS IP scattering corresponding to 0.38 Å^{-1} shows the diffraction spot for the EM image acquired at the edge of the domain but is absent for the image acquired at the centre of the domain, and *vice versa* is observed for $q = 0.33 \text{ Å}^{-1}$, as seen from the radial plot of FFT (Fig. 7). Moreover, the morphology at the center of the domains predominantly shows diffraction spots from lower spatial frequency ($k = 1/d$); however, at the edge of the domains, diffraction spots from the small and large k are present. Different molecular orientations can result in different

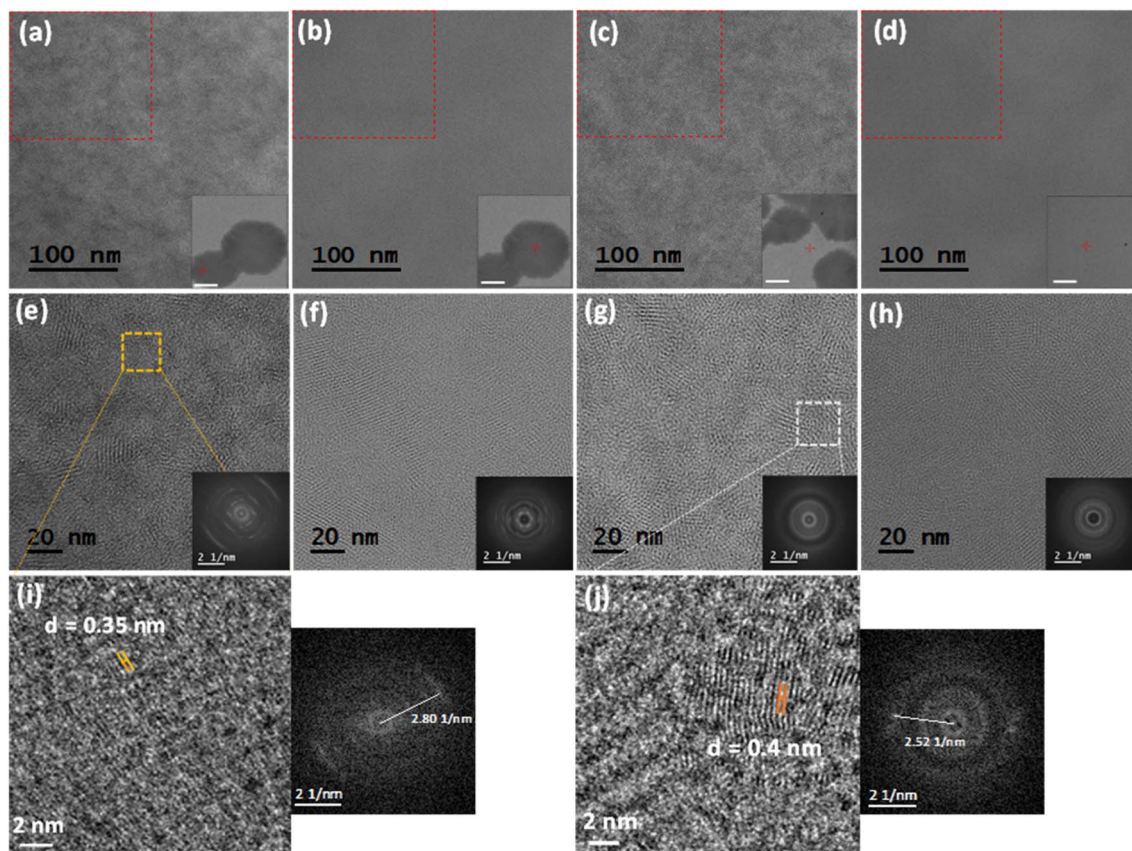


Fig. 6 Nanoscopic structural studies. High-magnification cryo-EM image of (a)–(c) coarse blend film and (d) fine blend film is taken at the cross-hairs of low-magnification image, which is shown at the inset of (a)–(d). Scale of the low-magnification image: 1 μm , scale of the high-magnification image: 100 nm. The zoomed high-magnification image (scale 20 nm) is obtained from the selected region of the (a)–(d) at the (e) edge of the domain, (f) center of the domain, (g) outside of the domains for the coarse film, and (h) fine blend film. FFT of the cryo-EM image (e)–(h) is represented as the image inset with a scale of 2 $1/\text{nm}$. (i) and (j) Zoomed high-magnification image (scale 2 nm) from the selected region in (e) and (g) showing fringes with a d -spacing of 0.35 nm and 0.4 nm, respectively. FFT of the images shows diffraction spots corresponding to the fringes (spatial frequency, $k = 1/d$ -spacing).

electrostatics, which can cause efficient charge dissociation in homojunction solar cells, as is observed for α -sexithiophene (6T).^{50,51} For α -6T, the orientation of molecules was altered by pre-patterning the substrates and evaporating 6T on them. However, a spin-coated film of **IEICO-4F** results in different molecular orientations because of its self-organization. Therefore, these materials could be an important candidate for solution-processable homojunction solar cells.

The high-magnification image from the outside region of the coarse film also shows crystalline fringes; however, the crystallinity is much lower than that in the inside region of the domains. Fig. S15[†] shows the FFT and its corresponding inverse FFT from a small area of the cryo-EM image that is acquired at the outside region of the domains. These local FFTs suggest that the materials in the outside region are also ordered and oriented in different directions, which is not evident from the FFT of the entire cryo-EM image. Moreover, Fig. S16[†] shows the presence of **PTB7-Th** and **IEICO-4F** crystallites in the matrix region, signifying that the matrix region also contains **IEICO-4F**.

Thus, the μ -Raman and cryo-EM results confirm that none of the regions are pure.

Fig. S17[†] shows the cryo-EM image and its FFT, and FFT from local regions, which enables visualizing the packing of materials in the **PTB7-Th:IEICO-4F** blend with fine morphology.

Fig. 8 shows the schematics of macroscopic, microscopic, and nanoscopic views of the **PTB7-Th:IEICO-4F** films that are spin-coated at 30 seconds and 120 seconds as evidenced by the X-ray scattering, AFM, KPFM, and cryo-EM experiments. The films that are spin-coated for 30 seconds dry slowly, self-assemble, and form a matte-finished film. This coarse film consists of large phase-separated domains that are rich in highly crystalline **IEICO-4F** with a capping layer of **PTB7-Th**, and a surrounding more disordered matrix that is rich in **PTB7-Th**. The films that are spin-coated for a full two minutes dry immediately, which results in shiny finished films with an optimized nanoscale blend morphology. Interestingly, different regions in the coarse blend film show different molecular orientations. The nanoscale morphology in the matrix region shows crystalline packing that is dominated by amorphous

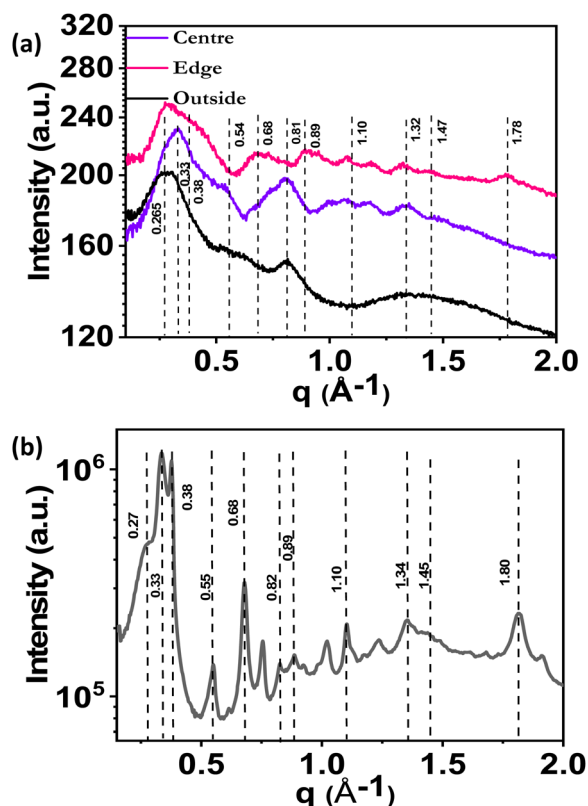


Fig. 7 Correlation of different structural studies. (a) Radial profiles of FFTs of cryo-EM images taken at domain center, domain edge, and outside domain for the coarse blend film. (b) 1-D IP GIWAXS profile for the coarse blend film.

regions of the material. The nanoscale morphology for the films that are spin-coated at 2 minutes shows fine, highly intermixed crystalline and amorphous domains of both materials, which

facilitates improved exciton dissociation and charge transport. Therefore, by combining various morphological and spectroscopic techniques, we have visualized the blend morphology at the nanoscale level, which shows how much drying conditions influence morphology and molecular ordering of NFAs.

Photovoltaic characteristics

To understand the effect of the observed processing condition-induced morphological changes on the device performance, solar cells were fabricated with an inverted device architecture of indium tin oxide (ITO)/zinc oxide (ZnO)/polyethylenimine ethoxylated (PEIE)/PTB7-Th: IEICO-4F/molybdenum oxide (MoO_x)/silver (Ag) with an effective area of 0.045 cm^2 . Devices were prepared with different donor-acceptor ratios in CB with $3 \text{ vol}\%$ 1-CN; the total concentration was maintained at 20 mg ml^{-1} (1:2, 1:1.5, and 1:1) and 15 mg ml^{-1} (2:1). Fig. S18† shows the digital and optical images of the devices to make sure that the blend film morphology is not affected by the device fabrication process. The dark and illuminated current-voltage (J - V) characteristics of the PTB7-Th:IEICO-4F in a 1:1.5 blend ratio for coarse and fine blend morphologies spin-coated at 2000 rpm are plotted in Fig. S19(a) and (b),† respectively. Films with coarse blend morphology show higher leakage current than films with fine morphology. Table 1 shows all the photovoltaic parameters: short circuit current density (J_{SC}), open circuit voltage (V_{OC}), fill factor (FF), J_{SC} calculated from external quantum efficiency (EQE), and mobilities measured using unipolar devices. Devices with coarse morphology show variation in performance from one device to another; therefore, the values presented in Table 1 are an average of 10 devices. Devices with coarse morphology show a power conversion efficiency (PCE) of 8% with a V_{OC} of 0.69 V, J_{SC} of 18.8 mA cm^{-2} , and FF of 62%. Increasing the spin-coating speed improves the PCE from

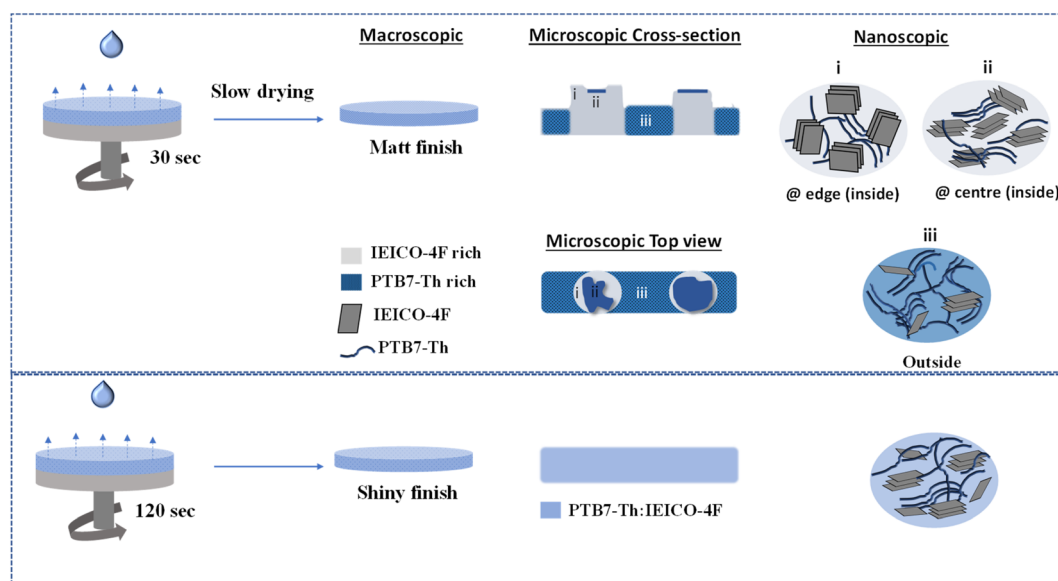


Fig. 8 Illustration of blend film morphology at different length scales. Schematic showing macroscopic, microscopic, and nanoscopic views of morphology for PTB7-Th:IEICO-4F films spin-coated at (a) 30 seconds and (b) 120 seconds. GIWAXS, cryo-EM, KPFM, and Raman spectroscopy data were combined to form the schematic.

Table 1 Summary of device performance parameters. Extracted device performance parameters from J - V and EQE measurements for coarse and fine films of **PTB7-Th:IEICO-4F** devices. Electron and hole mobility extracted from the J - V curve of single carrier devices for both films. Uncertainty is due to standard deviation of 10 samples

	J_{SC} (mA cm^{-2})	V_{OC} (V)	FF (%)	PCE (%)	J_{SC} from EQE (mA cm^{-2})	Electron mobility ($\text{cm}^2 \text{V}^{-1} \text{s}^{-1}$)	Hole mobility ($\text{cm}^2 \text{V}^{-1} \text{s}^{-1}$)
1 : 1.5 (coarse)	18.8 ± 2.2	0.69 ± 0.005	62 ± 1.1	8 ± 0.9 (8.9)	18 ± 2	$(0.61 \pm 0.4) \times 10^{-5}$	$(2.5 \pm 1) \times 10^{-3}$
1 : 1.5 (fine)	23.5 ± 0.4	0.72 ± 0.005	67 ± 0.2	11.3 ± 0.3 (11.6)	23	$(4.5 \pm 1) \times 10^{-5}$	$(2.2 \pm 0.9) \times 10^{-3}$

8 to 11.3%, which is primarily due to the increase in J_{SC} from 18.8 to 23.5 mA cm^{-2} along with a slight increase in FF and V_{OC} . It is interesting to note that although the processing conditions dramatically affect the morphology, its effect on device performance is relatively less. This result could be due to intermixing within the coarse domains in the large phase-separated morphology, as is observed from R-SoXS, which facilitates exciton dissociation within the phases. This contrasts with polymer/fullerene or polymer/polymer systems in which the current density and the FF reduce drastically, resulting in a reduction of PCE by more than 50% relative to optimized cells for devices with coarse phase-separated morphology.^{33,52,53} These results show that although the NFAs are sensitive to processing conditions due to their anisotropic chemical structures, the effect on their device performance is comparatively less; therefore, these systems can be a good candidate for printable and stable OSCs.

The EQE spectra of **PTB7-Th:IEICO-4F** solar cells with different morphologies are plotted in Fig. S19(c).† Similar to absorption spectra, the EQE spectra of devices with coarse morphology are red-shifted due to the aggregation of **IEICO-4F** in the blend. To maintain the consistency of spin speed, we have also fabricated the devices at 1500 rpm for 30 and 120 seconds as shown in Fig. S20.† The extracted device performance is summarised in Table S3.† The effect of morphology on the device performance is similar to the devices spin-coated at 2000 rpm. To understand the charge carrier recombination in the devices with coarse and fine morphology, intensity-dependent J - V is performed. Fig. S21† shows the intensity-dependent J_{SC} and V_{OC} plot and the results are discussed in ESI Note 3.† The results show that the fine blend morphology suppresses the geminate and the trap-assisted recombination, resulting in improved device FF and J_{SC} .

The dark J - V , illuminated J - V , and EQE of solar cells that are fabricated for different **PTB7-Th:IEICO-4F** blend ratios (1 : 2, 1 : 1, and 2 : 1) are shown in Fig. S22† and the extracted device parameters are summarised in Table S4.† To understand the effect of morphology on the charge transport of these devices, hole-only and electron-only devices were fabricated with the device architecture of ITO/PEDOT:PSS/**PTB7-Th:IEICO-4F**/MoO₃/Au and ITO/ZnO/PEIE/**PTB7-Th:IEICO-4F**/PFN-Br/Ag, respectively. The charge carrier mobility of the device can be improved by aggregation along with interconnecting pathways. Fig. S23† in the ESI† shows the dark J - V curve of electron-only and hole-only devices in the 1 : 1.5 blend ratio. The J - V plot of single carrier devices for other D-A ratios (1 : 2, 1 : 1, and 2 : 1) and extracted mobilities are shown in Fig. S24 and Table S5,†

respectively. The mobility calculation and the device performance for different donor-acceptor ratios are mentioned in ESI Note 4.† The electron mobility of devices with a coarse morphology is eight times lower than that of devices with fine morphology. The reduced electron mobility of the coarse blend film could be due to reduced interconnectivity of **IEICO-4F** molecules in the film. On the other hand, the hole mobility of coarse films is slightly higher than that of fine films, which could be due to, first, the presence of polymer aggregation along with interconnecting polymer chains in the coarse film; and second, the capping layer of pristine **PTB7-Th** on the large domains, which favors hole transport in a vertical direction.

To explore the effect of morphology evolution by the spin-coating process parameters beyond **PTB7-Th:IEICO-4F** blend system, we have performed the similar study on the high efficiency systems PM6:Y6 and PM6:Y7 bulk heterojunctions processed in different solvents. Fig. S25† shows that the absorption spectra and the morphology of PM6:Y6 and PM6:Y7 blend films strongly depend upon the spin-coating speed similar to **PTB7-Th:IEICO-4F**. Fig. S26† shows the μ -Raman spectra of pristine PM6, pristine Y6, pristine Y7, PM6:Y6, and PM6:Y7 blends. Similar to **PTB7-Th:IEICO-4F**, localization of Y6 and Y7 in the phase-separated domains of PM6:Y6 and PM6:Y7 blends, respectively, is observed. Therefore, these results indicate that this study of visualization of nanomorphology and the different orientational ordering can be generalized for other donor/NFA systems such as PM6:Y6 and PM6:Y7.

Conclusion

The thin film morphology of the **PTB7-Th:IEICO-4F** NFA blend is tuned *via* processing conditions from large phase-separated domains to fine domains. We have presented detailed studies to visualize the nanoscale multi-orientational molecular ordering in these tailored morphology-based blend films. Slow drying of the film results in large phase separation, with highly crystalline domains rich in **IEICO-4F** with a capping layer of **PTB7-Th** and a more disordered matrix rich in **PTB7-Th**. The drastic change in morphology and molecular packing in fine and coarse domains due to the processing conditions alters the absorption coefficient from $1.6 \times 10^5 \text{ cm}^{-1}$ to $7.5 \times 10^4 \text{ cm}^{-1}$ for **IEICO-4F** in the blend. Moreover, the morphology evolution of the BHJ system from micron-sized phase separated to nanoscale morphology is not only restricted to **PTB7-Th:IEICO-4F** and can be generalized to other high-performance systems, such as PM6:Y6 and PM6:Y7. Furthermore, the FFT of the cryo-EM images that are acquired at the edge and the center of the

domains in the coarse blend film shows that the molecules pack differently at both locations. To the best of our knowledge, these results have not been observed for spin-coated materials in the organic solar cell community before; therefore, they may provide useful insight to address unexpected observations for these NFAs, whether single-component OSCs and/or multiple CT rates. A comprehensive understanding of the molecular localization and ordering within the domain and matrix phases of spin-coated films is thus revealed using a combination of complementary microscopic, spectroscopic, and structural investigations. This study of the nano-morphology of NFA blends significantly improves the understanding of their aggregation and complex photophysics and provides fundamental insight into the opto-electronic characteristics of the film for further improving their device performance.

Experimental section

Thin film preparation: The studied systems were **PTB7-Th** (donor) and **IEICO-4F** (acceptor), which were purchased from 1-material and Solarmer, respectively, and used as-received. The M_w of **PTB7-Th** is ~ 180 kDa and PDI is ~ 2.5 . CB and 1-CN were purchased from Sigma-Aldrich. Glass slides, quartz, and silicon substrates were cleaned by sonicating them in soapy water, deionized water, acetone, and isopropyl alcohol for 10 minutes each. The substrates were dried using nitrogen; they were then placed in a plasma asher for 10 minutes to improve the wettability of the surface. Subsequently, the substrates were placed within a nitrogen-filled glove box. Solutions of 10 mg ml^{-1} of pristine **PTB7-Th** and pristine **IEICO-4F** were prepared in CB. Another 10 mg ml^{-1} solution of pristine **IEICO-4F** was prepared in CB with 3 vol% of 1-CN. The blend solution of a D-A ratio of 1 : 2 to 1 : 1 was prepared at 20 mg ml^{-1} in CB with 3 vol% of 1-CN. To keep the film thickness comparable to the film thickness of other blend ratios, when spin-coated at a particular rpm, the concentration of 2 : 1 and 4 : 1 blend was decreased to 15 mg ml^{-1} . All the solutions were stirred overnight at 60°C . The blend solution of PM6:Y6 (1 : 1.2) was prepared at 16 mg ml^{-1} in CF with 0.5 vol% 1-CN. The solution was stirred at room temperature inside a glove box. For PM6:Y7, the blend solution was prepared at 20 mg ml^{-1} in 1 : 1 ratio in CB with 2 vol% of 1-CN and stirred at 80°C . The blend solution was spin-coated at different speeds for different spin-coating durations. For UV-Vis absorption, Raman spectroscopy, and AFM characterization, the films of pristine material were spin-coated at 1500 rpm for 60 seconds on the glass substrate. The blend films of different donor-acceptor ratios were spin-coated at different speeds (1000, 1500, and 2000 rpm) for different spin-coating durations (30, 60, 90, and 120 seconds). Films for PL of pristine materials and the blend were prepared by spin-coating the solution on cleaned quartz substrates. For KPFM, reference substrate was formed by evaporating 50 nm of Au on ITO-coated glass substrates and blend films were formed by spin-coating a **PTB7-Th:IEICO-4F** (1 : 1.5) solution on the ITO-coated glass substrates. To find the work function of pristine donor and acceptor material, **PTB7-Th** solution was drop cast on one half, and pristine **IEICO-4F** on the other half of ITO-coated glass

substrate to form a lateral bilayer film. For GIWAXS, the cleaned Si substrates were spin-coated with pristine **PTB7-Th**, **IEICO-4F** and **IEICO-4F** with 1-CN solutions at 1500 rpm for 60 seconds. The 1 : 1.5 blend solution was spin-coated at 1500 rpm for 30 and 120 seconds. For cryo-EM and R-SoXS, NaPSS was spin-coated on the glass substrate and annealed at 120°C for 20 minutes. The **PTB7-Th:IEICO-4F** (1 : 1.5) solution was spin-coated at 1500 rpm for 30 and 120 seconds. The blend films were delaminated by floating them in water as NaPSS is a water sacrificial layer. The free-standing films were then transferred to copper mesh for cryo-EM characterization. For R-SoXS, the free-standing films were transferred to silicon nitride substrate.

PTB7-Th:IEICO-4F devices: PEIE, 2-methoxy ethanol, zinc acetate dihydrate, ethanolamine, and MoO_x were purchased from Sigma-Aldrich. The device was fabricated with an inverted architecture of ITO/ZnO/PEIE/**PTB7-Th:IEICO-4F**/ MoO_x /Ag. ITO-coated glass was purchased from Lumtec and cleaned with the procedure mentioned above. The cleaned ITO glass, after drying with nitrogen, was then placed in a plasma asher for 10 minutes. A 0.35 M ZnO solution was prepared by dissolving 1 g of Zn acetate dihydrate in 12.5 ml of 2-methoxy ethanol with 270 μl of ethanolamine, after which they were stirred overnight. The ZnO solution was spin-coated at 3000 rpm for 40 seconds and annealed at 200°C for 45 minutes. After annealing, the substrates were cooled down to room temperature. A PEIE solution with 0.2 wt% in 2-methoxyethanol was stirred overnight and spin-coated over the ZnO at 5000 rpm for 30 seconds; it was subsequently annealed at 100°C for 10 minutes. After deposition of the electron transport layers (ETL), the substrates were placed within a glove box. The different blend ratios of the **PTB7-Th:IEICO-4F** were spin-coated at 2000 rpm for 30 and 120 seconds. The spin-coated films were left to dry for some time (~ 15 minutes) in a N_2 atmosphere and then transferred to a thermal evaporator for 9 nm of MoO_x and 100 nm of Ag deposition at 3×10^{-6} mbar. The contacts to the devices were set by fixing leads at both ITO and Ag electrodes. Hole-only devices were fabricated with the device architecture, ITO/PEDOT:PSS/**PTB7-Th:IEICO-4F**/ MoO_3 /Au. The PEDOT:PSS (Clevis PH 1000) was purchased from Heraeus and spin-coated at 5000 rpm for 60 seconds and annealed at 150°C for 30 minutes in a N_2 atmosphere. The fabrication was followed by spin-coating active layer at different processing conditions, and deposition of 5 nm of MoO_x , and 40 nm of Au in a thermal evaporator. The electron-only devices were fabricated with the device architecture ITO/ZnO/PEIE/active layer/PFN-Br/Ag. The ETL and active layer were deposited in the same procedure as that in solar cell device fabrication. PFN-Br was purchased from solarmer and a solution of 0.5 mg ml^{-1} was prepared in methanol. The solution was stirred overnight at room temperature and then dynamically spin-coated at 2000 rpm. The device architecture was completed by depositing 100 nm of Ag.

Thin film morphology and spectroscopy: The UV-Vis-NIR absorption experiment was performed using a PerkinElmer Lambda 950 by placing the sample at the transmission port of the integrating sphere. The reflection by the sample in the UV-Vis-NIR region is measured by placing the sample at the end port of the integrating sphere and measuring the total reflection

by the sample. PL spectroscopy was performed on the pristine and the blend films by using a 638 nm TOPTICA-class 3B diode laser to excite the films that were kept in vacuum at a power of 0.25 mW, for the blend and pristine **IEICO-4F** that were with and without CN. A 650 nm-long pass filter was placed after the film to block the laser. The emission was collected using a Shamrock SR-303i spectrograph with an iDus 490 InGaAs charge couple device (CCD) from Andor. Height and phase AFM images for the pristine and blend films were recorded by using a MFP-3D from Asylum Research. The AFM was recorded for the $5\ \mu\text{m} \times 5\ \mu\text{m}$ window. KPFM images were also recorded in the dark using the same instrument in dual-pass mode under ambient conditions. Voltage was applied to the cantilever tip.

Cryo-EM was performed at the Ramaciotti Centre for Cryo-electron Microscopy using an FEI Titan Krios cryo-TEM operated at 300 kV and maintaining the specimen at liquid nitrogen temperature. Imaging was performed in bright-field TEM mode at a magnification of 165 kX. Phase-contrast high-resolution TEM images were collected at $-100\ \text{nm}$ defocus (lens spherical aberration $C_s = 2.7\ \text{mm}$) using a Gatan K2 camera (3838×3710) and a 10 eV energy filter slit to limit the contribution of inelastically scattered electrons. The electron illumination was set to 5.5 electrons/pixel/s. Each image consisted of the drift-corrected and aligned average of 50 frames at a dose of 1 electron/ $\text{\AA}^2/\text{frame}$. The image analysis was performed using GMS3 and imageJ software.

GIWAXS experiments were carried out at small- and wide-angle X-ray scattering beamline at Australian Synchrotron.⁵⁴ The samples were irradiated with 15 keV X-rays, with the images shown taken with an incident angle close to the critical angle that maximised scattering intensity. 2D GIWAXS patterns were recorded on a Pilatus3-2M detector (Dectris) placed $\sim 74\ \text{cm}$ downstream from the sample, with sample, detector, and entire beam path kept in a vacuum. Each scattering pattern was tiled together from three 1 second images with the detector slightly moved between exposures, such that the resulting image removes the gaps between the detector modules. The sample to detector distance was calibrated using a silver behenate scattering standard. Data were processed using a custom version of Nika implemented in IgorPro.⁵⁵

Raman characterization was performed using a WITec micro-Raman spectrometer with 632.8 nm excitation source. All the spectra were acquired at an incident power of 0.4 mW power, acquisition time of 25 seconds, numerical aperture of 0.9, and objective magnification of $50\times$. The approximate spot size of the laser was 800 nm. The polarization-dependent Raman spectroscopy was measured by changing the polarization angle of the circularly polarized light from -30° to 30° in the x - y plane. The Raman spectra for different polarization angles were collected using a 633 nm laser at a power of 0.4 mW for 30 seconds at the same position. The sample was checked after the experiment, and no degradation due to the laser was observed, thereby ruling out thermal effects in the observations. An optical image and video of film drying were collected using an Infinity camera mounted on an Olympus IX73 microscope ($60\times$, 0.71 NA) using Infinity capture software.

R-SoXS measurements were performed at the National Institute of Standards and Technology (NIST) Spectroscopy Soft and Tender (SST-1) beamline of the National Synchrotron Light Source II. R-SoXS patterns were measured at different photon energies, with an energy of 284.25 eV found to maximize material contrast. Samples were measured in a transmission configuration under vacuum with scattering recorded on a 2D CCD camera (Greateyes). 2D R-SoXS patterns were converted to 1D line profiles using a custom version of Nika, which was implemented in IgorPro.⁵⁵ Scattering was measured at two sample-to-detector positions; the data of low- q and high- q data stitched in the software. Certain commercial equipment, instruments, or materials (or suppliers, or software, *etc.*) are identified in this paper to foster understanding. Such identification does not imply recommendation or endorsement by the NIST, nor does it imply that the materials or equipment identified are necessarily the best available for the purpose.

Device characterization: Dark and illuminated current-voltage (J - V) measurements of the solar cell were performed using a Keithley 4200 semiconductor characterization system. The J - V curve for the electron- and hole-only devices was also measured with the same characterization tool. The devices were illuminated using a LED solar simulator from ORIEL, which was calibrated to 1 Sun condition ($100\ \text{mW cm}^{-2}$) at AM 1.5G. EQE was measured using a Bentham PVE300, which was composed of a dual lamp source (Xenon and quartz tungsten halogen lamp); the lamp was calibrated using a Si photodiode. The EQE measurement was performed in AC mode; therefore, EQE of the order 10^{-4} was recorded. The solar simulator intensity was varied by using different optical density filters and J - V was subsequently measured from the devices. The extracted J_{SC} and V_{OC} were plotted as a function of intensity for intensity dependent experiments.

Author contribution

U. B., D. K., C. R. M., and A. C. Y. L. designed the experiments. P. H. performed the micro-Raman spectroscopy experiment under the guidance of C. S. W. L. T. carried out the GIWAXS experiment and data analysis. E. G. performed the R-SoXS experiment and data analysis. H. V. and A. C. Y. L. performed the cryo-EM experiment. U. B. wrote the manuscript and performed rest of the experiments and data analysis. All the authors contributed to the manuscript. D. K., C. R. M., and A. C. Y. L. supervised the work.

Conflicts of interest

The authors have no potential conflicts to declare.

Acknowledgements

We acknowledge NCPRE and central facility, IITB for device fabrication and the characterizations facility. The authors acknowledge the use of instruments and assistance at the Monash Ramaciotti Centre for Cryo-Electron Microscopy, a Node of Microscopy Australia. This research used equipment funded

by the Australian Research Council grant (LE120100090). AL acknowledges support from the Australian Research Council (FT180100594). This work was performed in part at the SAXS/WAXS beamline at the Australian Synchrotron. This research also used the Spectroscopy Soft and Tender (SST-1) beamline of the National Synchrotron Light Source II, a U.S. Department of Energy (DOE) Office of Science User Facility operated for the DOE Office of Science by Brookhaven National Laboratory under contract no. DE-SC0012704. This work was supported by the Australia India Strategic Research Fund (AISRF53765). This work was also supported by the Indo-Swedish joint project funded by DST-India (DST/INT/SWD/VR/P-20/2019). This work was also supported by the Department of Science and Technology, Government of India through SwarnaJayanti Fellowship (DST/SB/SJF/2021-22/07-G dated January 23, 2020) and DST Women Scientist Scheme A (DST/WOS-A/CS-74/2019-G). D. K., C. S., U. B., and P. H. acknowledge financial support of the Ministry of Education, Government of India *via* IoE funding.

References

- 1 S. Li, C.-Z. Li, M. Shi and H. Chen, *ACS Energy Lett.*, 2020, **5**, 1554–1567.
- 2 Q. Liu, Y. Jiang, K. Jin, J. Qin, J. Xu, W. Li, J. Xiong, J. Liu, Z. Xiao, K. Sun, S. Yang, X. Zhang and L. Ding, *Sci. Bull.*, 2020, **65**, 272–275.
- 3 Y. Cui, Y. Xu, H. Yao, P. Bi, L. Hong, J. Zhang, Y. Zu, T. Zhang, J. Qin, J. Ren, Z. Chen, C. He, X. Hao, Z. Wei and J. Hou, *Adv. Mater.*, 2021, **33**, 2102420–2102427.
- 4 W. Li, M. Chen, J. Cai, E. L. K. Spooner, H. Zhang, R. S. Gurney, D. Liu, Z. Xiao, D. G. Lidzey, L. Ding and T. Wang, *Joule*, 2019, **3**, 819–833.
- 5 X. Xu, K. Feng, Y. W. Lee, H. Y. Woo, G. Zhang and Q. Peng, *Adv. Funct. Mater.*, 2020, **30**, 1907570–1907579.
- 6 X. Du, T. Heumueller, W. Gruber, A. Classen, T. Unruh, N. Li and C. J. Brabec, *Joule*, 2019, **3**, 215–226.
- 7 Z. Jiang, F. Wang, K. Fukuda, A. Karki, W. Huang, K. Yu, T. Yokota, K. Tajima, T. Q. Nguyen and T. Someya, *Proc. Natl. Acad. Sci. U. S. A.*, 2020, **117**, 6391–6397.
- 8 X. Song, N. Gasparini, L. Ye, H. Yao, J. Hou, H. Ade and D. Baran, *ACS Energy Lett.*, 2018, **3**, 669–676.
- 9 R. Wang, C. Zhang, Q. Li, Z. Zhang, X. Wang and M. Xiao, *J. Am. Chem. Soc.*, 2020, **142**, 12751–12759.
- 10 G. Zhang, X. K. Chen, J. Xiao, P. C. Y. Chow, M. Ren, G. Kupgan, X. Jiao, C. C. S. Chan, X. Du, R. Xia, Z. Chen, J. Yuan, Y. Zhang, S. Zhang, Y. Liu, Y. Zou, H. Yan, K. S. Wong, V. Coropceanu, N. Li, C. J. Brabec, J. L. Bredas, H. L. Yip and Y. Cao, *Nat. Commun.*, 2020, **11**, 3943–3953.
- 11 L. Perdigon-Toro, H. Zhang, A. Markina, J. Yuan, S. M. Hosseini, C. M. Wolff, G. Zuo, M. Stalterfoht, Y. Zou, F. Gao, D. Andrienko, S. Shoaee and D. Neher, *Adv. Mater.*, 2020, **32**, 1906763–1906772.
- 12 D. Li, X. Zhang, D. Liu and T. Wang, *J. Mater. Chem. A*, 2020, **8**, 15607–15619.
- 13 Z. Zhang, M. Li, Y. Liu, J. Zhang, S. Feng, X. Xu, J. Song and Z. Bo, *J. Mater. Chem. A*, 2017, **5**, 7776–7783.
- 14 M. Chen, D. Liu, W. Li, R. S. Gurney, D. Li, J. Cai, E. L. K. Spooner, R. C. Kilbride, J. D. McGettrick, T. M. Watson, Z. Li, R. A. L. Jones, D. G. Lidzey and T. Wang, *ACS Appl. Mater. Interfaces*, 2019, **11**, 26194–26203.
- 15 Z. Hamid, A. Wadsworth, E. Rezasoltani, S. Holliday, M. Azzouzi, M. Neophytou, A. A. Y. Guilbert, Y. Dong, M. S. Little, S. Mukherjee, A. A. Herzing, H. Bristow, R. J. Kline, D. M. DeLongchamp, A. A. Bakulin, J. R. Durrant, J. Nelson and I. McCulloch, *Adv. Energy Mater.*, 2020, **10**, 1903248.
- 16 X. Zhang, H. Wang, D. Li, M. Chen, Y. Mao, B. Du, Y. Zhuang, W. Tan, W. Huang, Y. Zhao, D. Liu and T. Wang, *Macromolecules*, 2020, **53**, 3747–3755.
- 17 G. Han, Y. Guo, X. Song, Y. Wang and Y. Yi, *J. Mater. Chem. C*, 2017, **5**, 4852–4857.
- 18 L. Ye, K. Weng, J. Xu, X. Du, S. Chandrabose, K. Chen, J. Zhou, G. Han, S. Tan, Z. Xie, Y. Yi, N. Li, F. Liu, J. M. Hodgkiss, C. J. Brabec and Y. Sun, *Nat. Commun.*, 2020, **11**, 6005–6014.
- 19 R. S. Gurney, D. G. Lidzey and T. Wang, *Rep. Prog. Phys.*, 2019, **82**, 036601–036638.
- 20 M. Chen, Z. Zhang, W. Li, J. Cai, J. Yu, E. L. K. Spooner, R. C. Kilbride, D. Li, B. Du, R. S. Gurney, D. Liu, W. Tang, D. G. Lidzey and T. Wang, *Sci. China: Chem.*, 2019, **62**, 1221–1229.
- 21 J. Chen, G. Li, Q. Zhu, X. Guo, Q. Fan, W. Ma and M. Zhang, *J. Mater. Chem. A*, 2019, **7**, 3745–3751.
- 22 X. Xu, L. Yu, H. Yan, R. Li and Q. Peng, *Energy Environ. Sci.*, 2020, **13**, 4381–4388.
- 23 K. Xian, Y. Liu, J. Liu, J. Yu, Y. Xing, Z. Peng, K. Zhou, M. Gao, W. Zhao, G. Lu, J. Zhang, J. Hou, Y. Geng and L. Ye, *J. Mater. Chem. A*, 2022, **10**, 3418–3429.
- 24 J. J. van Franeker, D. Westhoff, M. Turbiez, M. M. Wienk, V. Schmidt and R. A. J. Janssen, *Adv. Funct. Mater.*, 2015, **25**, 855–863.
- 25 Q. Li, L.-M. Wang, S. Liu, L. Guo, S. Dong, G. Ma, Z. Cao, X. Zhan, X. Gu, T. Zhu, Y.-P. Cai and F. Huang, *ACS Energy Lett.*, 2020, **5**, 3637–3646.
- 26 B. Schmidt-Hansberg, M. F. G. Klein, K. Peters, F. Buss, J. Pfeifer, S. Walheim, A. Colmann, U. Lemmer, P. Scharfer and W. Schabel, *J. Appl. Phys.*, 2009, **106**, 124501.
- 27 N. Li, J. D. Perea, T. Kassar, M. Richter, T. Heumueller, G. J. Matt, Y. Hou, N. S. Guldal, H. Chen, S. Chen, S. Langner, M. Berlinghof, T. Unruh and C. J. Brabec, *Nat. Commun.*, 2017, **8**, 14541–14550.
- 28 N. Jain, U. Bothra, D. Moghe, A. Sadhanala, R. H. Friend, C. R. McNeill and D. Kabra, *ACS Appl. Mater. Interfaces*, 2018, **10**, 44576–44582.
- 29 P. Westacott, J. R. Tumbleston, S. Shoaee, S. Fearn, J. H. Bannock, J. B. Gilchrist, S. Heutz, J. deMello, M. Heeney, H. Ade, J. Durrant, D. S. McPhail and N. Stingelin, *Energy Environ. Sci.*, 2013, **6**, 2756.
- 30 H. Fu, Z. Peng, Q. Fan, F. R. Lin, F. Qi, Y. Ran, Z. Wu, B. Fan, K. Jiang, H. Y. Woo, G. Lu, H. Ade and A. K. Jen, *Adv. Mater.*, 2022, **34**, e2202608.

- 31 J. Fang, Z. Wang, Y. Chen, Q. Zhang, J. Zhang, L. Zhu, M. Zhang, Z. Cui, Z. Wei, H. Ade and C.-Q. Ma, *Cell Rep. Phys. Sci.*, 2022, **3**, 100983.
- 32 L. Zhu, Q.-Z. Zhang, H. Ding, M. Zhang, X.-N. Xue, W.-K. Zhong, Z.-C. Zhou, J.-Q. Xu, W. Feng, Y.-C. Zou, Y.-M. Zhang and F. Liu, *Chin. J. Polym. Sci.*, 2022, 1–9.
- 33 U. Bothra, N. Jain, A. C. Y. Liu, A. Kala, W. Huang, X. Jiao, E. Gann, V. G. Achanta, C. R. McNeill and D. Kabra, *ACS Appl. Nano Mater.*, 2020, **3**, 11080–11089.
- 34 P. K. H. H. Ji-Seon Kim, C. E. Murphy and R. H. Friend, *Macromolecules*, 2004, **37**, 2861–2871.
- 35 B. A. Collins, Z. Li, J. R. Tumbleston, E. Gann, C. R. McNeill and H. Ade, *Adv. Energy Mater.*, 2013, **3**, 65–74.
- 36 B. W. Christopher, R. McNeill, L. Thomsen, W. J. Belcher, N. C. Greenham and P. C. Dastoor, *Nanoletters*, 2006, **6**, 1202–1206.
- 37 M. Schubert, B. A. Collins, H. Mangold, I. A. Howard, W. Schindler, K. Vandewal, S. Roland, J. Behrends, F. Krafft, R. Steyrleuthner, Z. Chen, K. Fostiropoulos, R. Bittl, A. Salleo, A. Facchetti, F. Laquai, H. W. Ade and D. Neher, *Adv. Funct. Mater.*, 2014, **24**, 4068–4081.
- 38 W. Köntges, P. Perkhun, J. Kammerer, R. Alkarsifi, U. Würfel, O. Margeat, C. Videlot-Ackermann, J.-J. Simon, R. R. Schröder, J. Ackermann and M. Pfannmöller, *Energy Environ. Sci.*, 2020, **13**, 1259–1268.
- 39 J. Liu, Z. Li, J. Wang, X. Zhang, X. Zhan and G. Lu, *J. Mater. Chem. A*, 2020, **8**, 23304–23312.
- 40 Y. Zhu, A. Gadisa, Z. Peng, M. Ghasemi, L. Ye, Z. Xu, S. Zhao and H. Ade, *Adv. Energy Mater.*, 2019, **9**, 1900376.
- 41 L. B. r. Marco Chiesa, J.-S. Kim, R. Shikler, R. H. Friend and H. Sirringhaus, *Nano Lett.*, 2005, **5**, 559–563.
- 42 M. Elshobaki, R. Gebhardt, J. Carr, W. Lindemann, W. Wang, E. Grieser, S. Venkatesan, E. Ngo, U. Bhattacharjee, J. Strzalka, Z. Jiang, Q. Qiao, J. Petrich, D. Vaknin and S. Chaudhary, *ACS Appl. Mater. Interfaces*, 2017, **9**, 2678–2685.
- 43 V. Palermo, M. Palma and P. Samori, *Adv. Mater.*, 2006, **18**, 145–164.
- 44 H. Hoppe, M. Niggemann, C. Winder, J. Kraut, R. Hiesgen, A. Hinsch, D. Meissner and N. S. Sariciftci, *Adv. Funct. Mater.*, 2004, **14**, 1005–1011.
- 45 S. Kim, M. A. M. Rashid, T. Ko, K. Ahn, Y. Shin, S. Nah, M. H. Kim, B. Kim, K. Kwak and M. Cho, *J. Phys. Chem. C*, 2020, **124**, 2762–2770.
- 46 L. Ye, Y. Xiong, M. Zhang, X. Guo, H. Guan, Y. Zou and H. Ade, *Nano Energy*, 2020, **77**, 105310–105321.
- 47 W. Huang, E. Gann, L. Thomsen, C. Dong, Y.-B. Cheng and C. R. McNeill, *Adv. Energy Mater.*, 2015, **5**, 1401259.
- 48 P. H. H. B. Maarten, J. M. Wirix, H. Friedrich, N. A. J. M. Sommerdijk and G. de With, *Nano Lett.*, 2014, **14**, 5.
- 49 E. J. Kirkland, *Advanced Computing in Electron Microscopy*, Springer, US, 2nd edn, 2010.
- 50 Y. Dong, V. C. Nikolis, F. Talnack, Y. C. Chin, J. Benduhn, G. Londi, J. Kublitski, X. Zheng, S. C. B. Mannsfeld, D. Spoltore, L. Muccioli, J. Li, X. Blase, D. Beljonne, J. S. Kim, A. A. Bakulin, G. D'Avino, J. R. Durrant and K. Vandewal, *Nat. Commun.*, 2020, **11**, 4617–4626.
- 51 S. Duhm, G. Heimel, I. Salzmann, H. Glowatzki, R. L. Johnson, A. Vollmer, J. P. Rabe and N. Koch, *Nat. Mater.*, 2008, **7**, 326–332.
- 52 Y. Liang, Z. Xu, J. Xia, S. T. Tsai, Y. Wu, G. Li, C. Ray and L. Yu, *Adv. Mater.*, 2010, **22**, E135–E138.
- 53 L. Zhu, W. Zhong, C. Qiu, B. Lyu, Z. Zhou, M. Zhang, J. Song, J. Xu, J. Wang, J. Ali, W. Feng, Z. Shi, X. Gu, L. Ying, Y. Zhang and F. Liu, *Adv. Mater.*, 2019, **31**, 1902899–1902908.
- 54 N. M. Kirby, S. T. Mudie, A. M. Hawley, D. J. Cookson, H. D. T. Mertens, N. Cowieson and V. Samardzic-Boban, *J. Appl. Crystallogr.*, 2013, **46**, 1670–1680.
- 55 J. Ilavsky, *J. Appl. Crystallogr.*, 2012, **45**, 324–328.
- 56 L. Zhu, M. Zhang, J. Xu, C. Li, J. Yan, G. Zhou, W. Zhong, T. Hao, J. Song, X. Xue, Z. Zhou, R. Zheng, H. Zhu, C.-c. Chen, R. C. I. MacKenzie, Y. Zou, J. Nelson, Y. Zhang, Y. Sun and F. Liu, *Nat. Mater.*, 2022, **21**, 656–663.